Strategies to challenge the simulation of confined fires

F. Salmon [a,*], J.-C. Mindeguia [a], D. Lacanette [a], C. Sirieix [a], J.-C. Leblanc [b], C. Ferrier [c]

[a] Université de Bordeaux, CNRS, ENSAM, Bordeaux-INP, INRA, UMR 5295 I2M, 33405 Talence, France
[b] Université de Toulouse, UMR CNRS 5608 TRACES, 31058 Toulouse, France
[c] Université de Bordeaux, UMR CNRS 5199 PACEA, 33600 Pessac, France

Keywords:
FireFOAM
Ceiling jet
Compartment fire
Combustion
Confined
Tunnel

A B S T R A C T

The numerical simulation of fires concerns an increasingly wide range of applications, among which archaeology. The Chauvet-Pont d'Arc Cave (France) presents thermal marks on some of its walls. These marks result from prehistorical fires and archaeologists would like to know their characteristics (fire location, mass of fuel, number of fires, etc) to make assumptions about their functions. Being impossible to carry out fires in the cave, combustion simulation is a suitable tool to discuss this question. However, simulating a fire in a confined geometry is still challenging and some inherent difficulties must be overcome. In that respect, we reproduced four experimental fires in a cave-like geometry. Four tepee-like hearths, composed of different initial wood masses (16, 32, 60 and 90 kg), were burnt in an underground quarry. Twenty-seven thermocouples measured the temperature in the cold and hot gas layers, as well as in the ceiling jet area. The measurements in the ceiling jet resulting from the 90 kg fire are successfully compared to the corrected Delichatsios correlations. In addition, the measured mass loss rate is compared to a tailored modeling for tepee hearths. We also propose three strategies to simulate the combustion process of the 90 kg hearth: (i) with a significant refinement in the ceiling jet area (approximately 1,500,000 cells) and the law of the wall, (ii) without refinement but with Newton's law of cooling and (iii) without refinement but with simplifying assumptions and adjustments. While the first and third approaches provide meaningful results, the second case is found to be inconvenient for compartment fires. Based on experimental data, this study aims to give some keys to perform simulations of compartment fires (in tunnels, buildings, car parks, etc) and numerically approximate the combustion of wood.

1. Introduction

Numerical simulation allows scientists to predict or reproduce physical phenomena. Ever-increasing computing performance broadens the research spectrum to more complex and coupled processes. Fire engineering is then more and more subject to researches in numerical simulation. For instance, the fires in tunnels are widely studied for safety reasons (Ingason et al., 2015). As Chen et al. (2020), Yao et al. (2018) focused on the temperature beneath a ceiling during a tunnel fire. Similarly, authors investigate compartment fires and often compare Computational Fluid Dynamics (CFD) simulations with experimental data. Betting et al. (2018) investigated the smoke dynamics of a compartment fire with FDS (Fire Dynamics Simulator) (McGrattan et al., 2013). This code was also used by He et al. (2018) to simulate the gas circulation in a vented compartment. Other codes such as FireFOAM (FireFOAM, 2020) can similarly manage this kind of investigation (Salmon et al., 2018; Le et al., 2018). Beyond considerations on temperature, velocity or gas concentration, confinement adds further difficulties. Among others, the ceiling jet phenomenon has been thoroughly analyzed for 40 years. This shallow gas layer beneath a ceiling was first investigated from an experimental point of view by many authors such as Alpert (Alpert, 1975) or Delichatsios (Delichatsios, 1981) before being studied numerically (Huo et al., 2015; Liu et al., 2016; Hara and Kato, 2006; Ye et al., 2019; Tang et al., 2020). Chatterjee et al. (2017) compared simulation with empirical correlations for inclined ceilings (Oka and Ando, 2013) and experimental data. Zadeh et al. (2016) compared their own data to simulations. Both studies were based on FireFOAM but FDS was also adopted in this context (Johansson et al., 2015). The ceiling jet phenomenon is also encountered in tunnel fires. This field, which often falls in the scope of fire safety, is widely studied numerically. Fires stemming from vehicles in tunnels are investigated in (Caliendo et al., 2013) and (Hsu et al., 2017). The hazard due to smoke is also a key issue in tunnels (Zhao et al., 2018; Meng et al., 2014).

These researches fall within contemporary matters but fire science

* Corresponding author at: Université de Bordeaux, UMR CNRS 5295 I2M, 16 Avenue Pey Berland, Pessac, France.
E-mail address: Salmon.Fabien@yahoo.com (F. Salmon).

https://doi.org/10.1016/j.tust.2020.103806

can also contribute to archaeological issues. In the Chauvet-Pont d'Arc Cave (France), one of the most famous painted caves in the world, some anthropogenic thermal marks challenge archaeologists (Brodard et al., 2014; Debard et al., 2012). Some walls present color changes (red and gray) resulting from high-temperature chemical reactions (Walter et al., 2001; Brodard et al., 2014), spalling (Mindeguia et al., 2015) and soot deposits. These features suggest that fires occurred deep in the cave between 37,000 and 33,500 years ago (Quiles et al., 2016; Guibert et al., 2015). Moreover, the fires' intensity appears unusual and the functions classically attributed to the archaeological fires seem irrelevant (Ferrier et al., 2014). For conservation reasons, numerical simulation is the most appropriate approach to advance in the understanding of these singular fires: wood quantity, hearth arrangement, locations, number of fires, etc. This paper takes part in the construction of a numerical model capable of characterizing these archaeological fires and follows the prior works (Lacanette et al., 2017; Salmon et al., 2019a,b).

First, four experimental fires, carried out in a former underground limestone quarry, are described. One objective of these experiments is to develop a heat release source modeling for tepee-like hearths. In the Chauvet-Pont d'Arc Cave, *Pinus* sp. was burnt (Théry-Parisot et al., 2018) and the hearths were probably arranged in tepee-type structures. To cover a large enough fuel mass range consistent with the archaeological purposes, four masses (16.8, 40, 60 and 90 kg) were successively burnt. A weighing balance measured the mass loss rate of wood during the fires. Moreover, the quarry was instrumented by thermocouples in the hot and cold gases, in addition to the ceiling jet area near the fire.

Second, the theoretical background required in the study is outlined. The empirical wood crib method is described from a mathematical point of view. Inspired by this approach, we propose a modeling for the HRR (Heat Release Rate) of our tepee-like structures. As regards ceiling jet, given the power released by the fires, only Delichatsios' correlation (Delichatsios, 1981) has been found to be applicable to the quarry geometry which is composed of two corridors (Beyler, 1986). This formulation is thus provided to compare it with the measurements. The numerical tool FireFOAM is only presented briefly since a deeper description has already been published (Salmon et al., 2019a,b). The confrontation between experiment and simulation is made through different numerical configurations (mesh and convective heat transfer modeling). The modelings involved in each case are specified.

Finally, the results about the mass loss rate, the thermal ambiance in the quarry and the ceiling jet are confronted with the experimental data for the 90 kg hearth. One hearth is chosen for the comparison to avoid being repetitive. In particular, we present the results of three different simulations to show the pros and cons of each of them. The impact of the refinement of the ceiling jet area is investigated and we show its necessity for this study. Big meshes making simulations time-consuming, we applied simplifying assumptions developed in a prior paper (Salmon et al., 2019a,b) to the simulation of the 90 kg hearth.

2. Experiments

The experiments relate to the combustion of tepee-shaped wood hearths in a former limestone quarry in Lugasson (Gironde, France). The quarry is a right-angle gallery that leads to the outside (Fig. 1). The fuel was burnt 80 cm from the back of the quarry in gallery 2 where there are 2.5 m in height under the ceiling. The combustion of four tepee hearths composed of different wood masses (16.8 kg, 40 kg, 60 kg and 90 kg) was achieved (Fig. 2). The ignition was performed by a blowtorch with several heating points in the hearths. Each fire occurred on different days with similar thermal conditions in the quarry and outside (about 12 °C). The dioxygen supply was sufficient to avoid extinguishment while there was still wood. The low distance between the fire location and the entrance in comparison with the area of the opening seems to have allowed this fuel-controlled combustion (Yao et al., 2019).

The quarry was instrumented with 27 shielded type-K thermocouples. Each triangle in Fig. 3 corresponds to a vertical tree of thermocouples that consists in vertically distant thermocouples of 0.5 mm diameter. These thermocouples are located in the hot and cold gas layers but also in the ceiling jet area. Their vertical positions are presented in Fig. 4. Under the fire burning site, a weighing scale measured the fuel mass during each combustion process. This allows the mass flow rate calculation. The heat release rate is deduced by assuming that the heat of combustion remains constant (12.5 MJ.kg^{-1}).

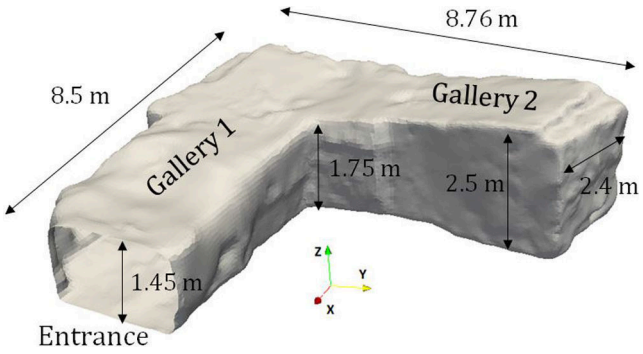

Fig. 1. Geometry of the quarry acquired by photogrammetry (P. Mora, Archéovision Production).

3. Theory

3.1. HRR model

This part deals with the development of a HRR model for our tepee-like wooden hearths. Fig. 5 displays the conventional curve for HRR. Considering the trend of the measured HRR in our experiments (Fig. 7), we will adjust this kind of curve on the measurements. However, the linear decrease of the fuel surface-controlled regime is replaced with an exponential law to better fit the measurements (see Section 4.1) like in (Ingason, 2009). The corresponding mass loss rate is then given by $\dot{m}_{Fuelsurface} = \beta e^{-\alpha t}$.

Based on the experiments, the mass loss rate is given by:

$$\dot{m} = \begin{cases} [694.64 m_0 + 63370]^{-1.6} m_0 t^2 & \text{if } t < 375 \ s \\ \min\left(\dot{m}_1, \dot{m}_2\right) & \text{otherwise} \end{cases} \qquad (1)$$

$$\dot{m}_1 = \beta e^{-\alpha t}$$

$$\dot{m}_2 = \frac{-3.53 \times 10^{-9} m_0^2 + 9.41 \times 10^{-8} m_0 + 8.41 \times 10^{-5}}{3.8 \times 10^{-4} m_0 + 0.03515} m_0$$

3.2. Ceiling jet

In a confined space, the rising hot gases that result from a fire impinge on the ceiling. Due to this obstacle, the flow turns and escapes horizontally. The ceiling jet corresponds to the quick and thin gas layer under the ceiling. According to Alpert (Alpert, 2016), this only exists at the beginning of the combustion process while no stagnant hot layer takes place beneath it.

Some empirical formulations concern the maximum temperature in ceiling jets (Beyler, 1986). Considering the confinement of the geometry (Fig. 1), only Delichatsios' correlation (Delichatsios, 1981) can estimate the maximum temperature of the ceiling jet in the quarry:

$$T - T_\infty = 0.29 \Delta T_m \left(\frac{H}{l_b}\right)^{\frac{1}{3}} exp\left[-0.2 \frac{Y}{H} \left(\frac{l_b}{H}\right)^{\frac{-1}{3}}\right] \qquad (2)$$

with T_∞ the ambient temperature, H the ceiling height above the burning site, l_b the corridor half-width, Y the distance along the gallery from the source and ΔT_m the temperature difference (with the ambient

temperature) at the ceiling above the source center. The latter can be calculated from the correlation (Alpert, 2016) $\Delta T_m = 6.3 T_\infty \dot{Q}_c^{*2/3}$ with $\dot{Q}_c^* = \frac{\dot{Q}_c}{\rho_\infty c_{p,\infty} T_\infty \sqrt{g} H^{\frac{5}{2}}}$, $\dot{Q}_c$ the HRR (kW), ρ_∞ the ambient density, $c_{p,\infty}$ the specific heat at constant pressure ($kJ.kg^{-1}.K^{-1}$) and g Earth's gravity. For the quarry, Eq. (2) is valid on the range $Y \in [1.6; 9.5]$m. Note that the quarry ceiling is slightly inclined (Fig. 1) contrary to Delichatsios' hypotheses.

Although the definition of ceiling jet given by Alpert does not consider any hot layer, some authors investigated the impact of hot gases on the temperature of ceiling jets. This is of great interest here because there were hot layers during the experimental fires (Section 2). Instead of creating new correlations, Cooper (1984) and Evans (1985) introduced corrections that affect $.Q_C$ and H in the existing correlations. Even with a hot layer, Delichatsios' correlation can thus be used with the modified $.Q_C$ and H. With Z_I the vertical distance between the layers interface and the hearth, $\dot{Q}_I^* = \frac{\dot{Q}_c}{\rho_\infty c_{p,\infty} T_\infty \sqrt{g} Z_I^{\frac{5}{2}}}$, $C_T = 9.115$, $\beta^2 = 0.913$ and $\xi = \frac{T_{Hot}}{T_\infty}$ (the subscript "Hot" means hot layer), the corrections are:

3.3. Numerical description

3.3.1. Numerical solver

FireFOAM-4.0 manages the Large Eddy Simulation (LES) of fluids and fires. The code is thoroughly described in (Salmon et al., 2019a,b) so only an overview is presented here. This tool is based on the Favre averaged Navier-Stokes equations and convection–diffusion equations for all the chemical species taking part in the combustion process. The Lewis number is supposed to be equal to one (common assumption (McGrattan et al., 2013)). The species and temperature turbulent fluxes are closed thanks to a gradient transport hypothesis. The turbulence model (Yoshizawa, 1986) consists of one differential equation on the subgrid-scale kinetic energy (3) and an empirical formulation for the eddy viscosity $\nu_t = C_k \sqrt{k} \Delta$ with $C_k = 0.094$

$$\begin{aligned} \partial \rho k / \partial t + \partial \rho \widetilde{u_j} k / \partial x_j - \partial / \partial x_j \left[\mu_{eff} \partial k / \partial x_j \right] = -2/3 \rho k \partial \widetilde{u_k} / \partial x_k + \\ \mu_{eff} \partial \widetilde{u_i} / \partial x_j \left(2 S_{ij} - 2/3 S_{kk} \delta_{ij} \right) - C_\epsilon \rho k^{3/2} / \Delta \end{aligned} \tag{3}$$

where Δ is the filter size directly linked to size mesh and $C_\epsilon = 1.048$.

Cooper (Cooper, 1984)	Evans (Evans, 1985)
$\sigma = \left(\frac{\xi}{\xi - 1}\right)\left[\frac{1 + C_T \dot{Q}_I^{*\frac{2}{3}}}{\xi} - 1\right]$	$\dot{Q}_{I,2}^* = \left(\frac{1 + C_T \dot{Q}_I^{*\frac{2}{3}}}{\xi C_T} - \frac{1}{C_T}\right)^{3/2}$
$m_2^* = \frac{1.04599\sigma + 0.360391\sigma^2}{1 + 1.37748\sigma + 0.360391\sigma^2}$	
$Z_{I,2} = Z_I \xi^{\frac{3}{5}} m_2^{*\frac{2}{5}} \left(\frac{1+\sigma}{\sigma}\right)^{1/3}$	$Z_{I,2} = Z_I \left\{ \frac{\xi \dot{Q}_I^* C_T}{\dot{Q}_{I,2}^{*\frac{1}{3}} \left[(\xi - 1)(\beta^2 + 1) + \xi C_T \dot{Q}_{I,2}^{*\frac{2}{3}} \right]} \right\}^{2/5}$
$\dot{Q}_{c,2} = \dot{Q}_c \frac{\sigma}{\sigma + 1} m_2^*$	$\dot{Q}_{c,2} = \dot{Q}_{I,2}^* \rho_{\infty,Hot} c_{p,Hot} T_{Hot} \sqrt{g} Z_{I,2}^{5/2}$
$H_2 = H - Z_I + Z_{I,2}$	

Subscript 2 refers to the corrected variables. In Delichatsios' correlation, H must be replaced by H_2 and $\dot{Q}_c$ by $\dot{Q}_{c,2}$.

The radiation in the quarry is calculated from the finite volume discrete ordinary method (fvDOM). This technique corresponds to the resolution of the radiative transfer equation over the whole geometry in N directions. We choose $N = 32$ in this study since it was found to be suffi-

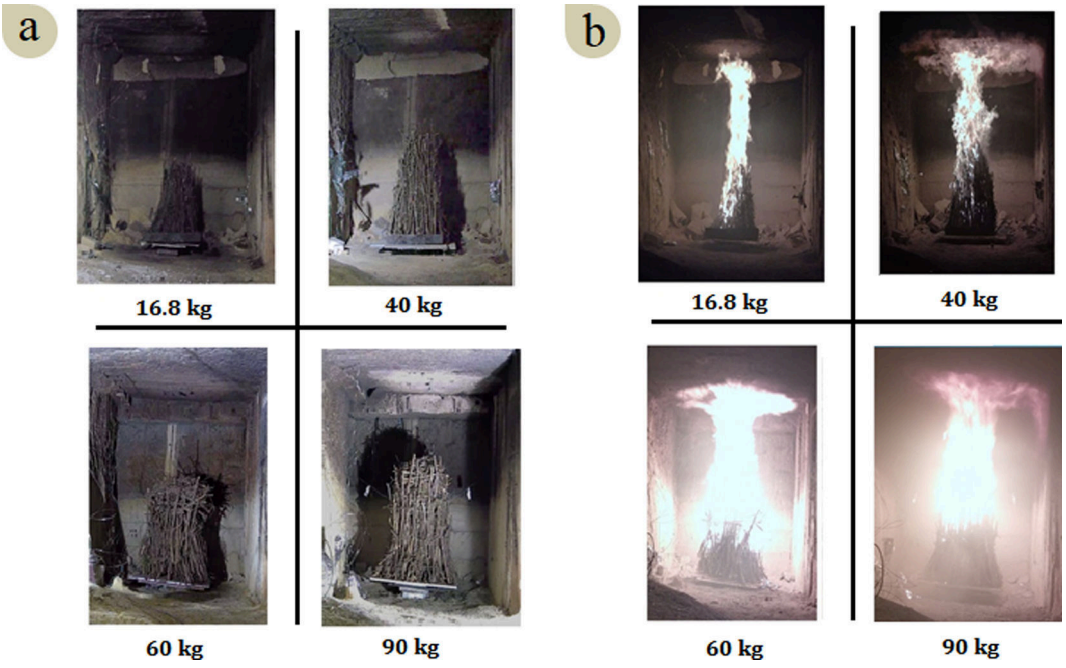

Fig. 2. a, Initial hearths of different masses (16.8, 40, 60 and 90 kg) on a weighing scale (J.C. Mindeguia). b, Hearths during the fires (J.C. Mindeguia).

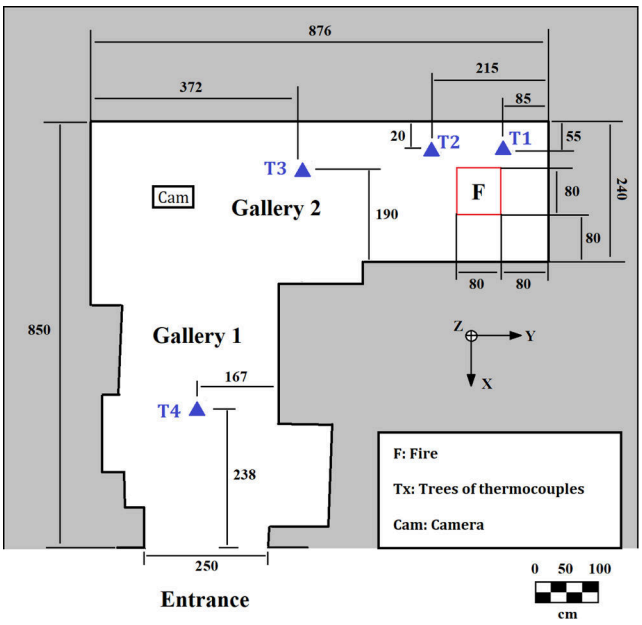

Fig. 3. Cutaway view of the instrumented quarry with the camera and vertical trees of thermocouples.

cient (Salmon, 2019). The combustion process of wood is modeled by the eddy dissipation model (Magnussen and Hjertager, 1977). The reaction is assumed to follow the chemical reaction

$$Wood + 0.4028O_2 + 1.516N_2 = 0.3609CO_2 + 0.8647H_2O + 0.0084CO + 1.516N_2$$

The thermocouple temperature correction satisfies the corresponding equation provided in (Salmon et al., 2019a,b). Considering the complexity of the involved phenomena, we developed in (Salmon et al., 2019a,b) a simplifying assumption about the vertical component of the velocity. Outside the turning region, the vertical velocity of the gases in the quarry is assumed to be equal to zero. We refer to (Salmon et al., 2019a,b) for further information. This assumption will only be used for the simulation presented in Section 4.3.3.

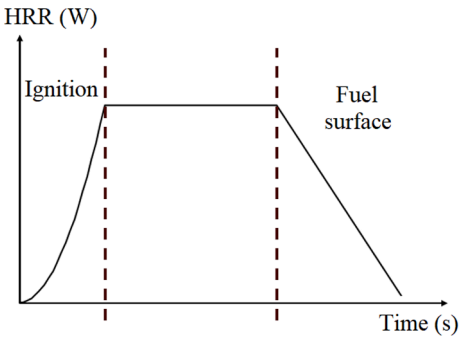

Fig. 5. Conventional HRR (Heat Release Rate) curve (ventilation is assumed to be non-limiting).

3.3.2. *Convective heat transfer*

Convective heat transfer relates to energy losses through boundary layers from millimeters to more than one centimeter. Let us introduce the friction velocity $u^* = \sqrt{\frac{\tau_w}{\rho}}$ with τ_w the wall shear stress and ρ the fluid density at the wall, and a non-dimensional wall distance $y^+ = \frac{u^* y}{\nu}$ with y the distance to the nearest wall and ν the local kinematic viscosity of the fluid. This phenomenon is a critical point in CFD (Computational Fluid Dynamics) simulations and can be managed with different methods. The most accurate one corresponds to DNS (Direct Numerical Simulation) and needs a very fine mesh ($y^+ \sim 1$ and enough cells in the boundary layer). For 3D simulations, this approach is very time-consuming and often not suitable. Instead, most of CFD simulations are based on

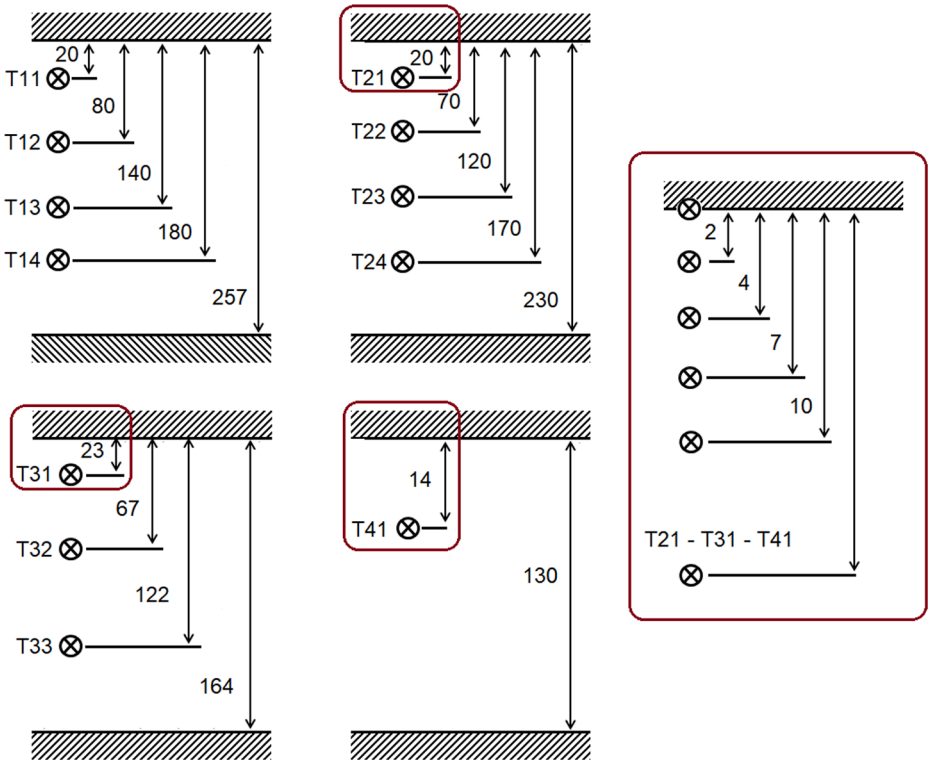

Fig. 4. Vertical locations of the thermocouples for each tree. For trees T2, T3 and T4, the sensors are identically positioned in the ceiling jet area. The distances are given in cm.

Newton's law of cooling $q = h(T_w - T_g)$ where h is the convective heat transfer coefficient, T_w is the wall temperature and T_g is the gas temperature. The estimation of the convective heat transfer coefficient depends on the mesh refinement. In this study, we confront three strategies.

(i) When the center of the boundary cells is inside the boundary layer but not close enough to the walls to perform a DNS calculation, the law of the wall must ensure the modeling of the fluid variables at the boundary. For velocity, the Spalding law (Spalding, 1961) is used

$$y^+ = u^+ + \frac{1}{E}\left[e^{\kappa u^+} - 1 - \kappa u^+ - \frac{(\kappa u^+)^2}{2} - \frac{(\kappa u^+)^3}{6}\right] \tag{4}$$

where $u^+ = \frac{u(y)}{u^*}$, $\kappa = 0.41$ is the von Kàrmàn constant and $E = 9.8$.

The eddy viscosity is then derived from $u^{*2} = \nu_t \nabla u.n$ with n the wall-normal vector. For temperature, let us first introduce two other variables: $T_\tau = \frac{Dq}{\lambda u^*}$ and $T^* = \frac{T_w - T_g}{T_\tau}$ with D the thermal diffusivity of the gas at the boundary. Therefore, the convective heat transfer coefficient is given by $h = \frac{\lambda u^*}{DT^*}$ and

$$T^* = \begin{cases} y^+ Pr + \frac{1}{2}\frac{\rho u^* u^2 Pr}{q} if \;\; y^+ < y_T^+ \\ \mathrm{Pr}_t\left[\frac{1}{\kappa}\ln(Ey^+) + P\right] + \frac{1}{2}\frac{\rho u^*}{q}\left\{Pr_t u^2 + (Pr - Pr_t)u_c^2\right\} if \;\; y^+ > y_T^+ \end{cases} \tag{5}$$

with u_c the velocity when $y^+ = y_T^+$ and $y_T^+ = \frac{Pr_t}{Pr}\left(\frac{1}{\kappa}\ln(Ey_T^+) + P\right)$. P is provided by the Jayatilleke function (Jayatilleke, 1969) $P = 9.24\left[\left(\frac{Pr}{Pr_t}\right)^{\frac{3}{4}} - 1\right]\left[1 + 0.28e^{-0.007\frac{Pr}{Pr_t}}\right]$.

With access to high-performance computing facilities, this approach becomes possible for relatively large 3D geometries such as the quarry (Fig. 1).

(ii) When the size of the boundary cells is such that their centers are outside the boundary layer, the following analytical correlations for plane surfaces can be employed (Holman, 2010)

$$h = \frac{\lambda}{L}\begin{cases} 0.66 Pr^{\frac{1}{3}} Re^{\frac{1}{2}} if \;\; Re < 5 \times 10^5 \\ 0.037 Pr^{\frac{1}{3}} Re^{0.8} if \;\; 5 \times 10^5 < Re < 10^7 \end{cases} \tag{6}$$

where λ is the thermal conductivity of the gas at the boundary, L is a characteristic length usually equal to one, Pr is the Prandtl number and $\Re$ is the Reynolds number.

(iii) In a previous article (Salmon et al., 2019a,b), formulation (6) was tailored to fit to experiments in the above-mentioned quarry. It consists in modifying the characteristic length according to the gas temperature. This adjustment was required mainly because there was no refinement at the boundaries. At the ceiling, the same empirical heat transfer as in (Salmon et al., 2019a,b) is used. Like both previous formulations (i) and (ii), these customized correlations will be confronted with the experimental data of the 90 kg hearth (Section 2).

3.3.3. Numerical setup

The meshing process of the quarry (Fig. 6a) is performed with cfMesh (cfMesh, 2020). For the three convective transfer methods, 3 cm cubic cells mesh the flame area while the remaining mesh is composed of 6 cm cubic cells. A coarse-mesh block ($20 \times 20 \times 80$ m^3), corresponding to the outside, joins the quarry exit to avoid any boundary issue. For the first method (i), the mesh must be refined under the ceiling. First, a thickness of about 4.5 cm is meshed with 7.5 mm cubic cells (correspond to y^+~15). Then, a layer at least 20 cm thick is meshed with 3 cm cubic cells (Fig. 6b). In addition, the experimental hearth is approximated with a pyramid shape (Fig. 6c). The HRR boundary condition is only

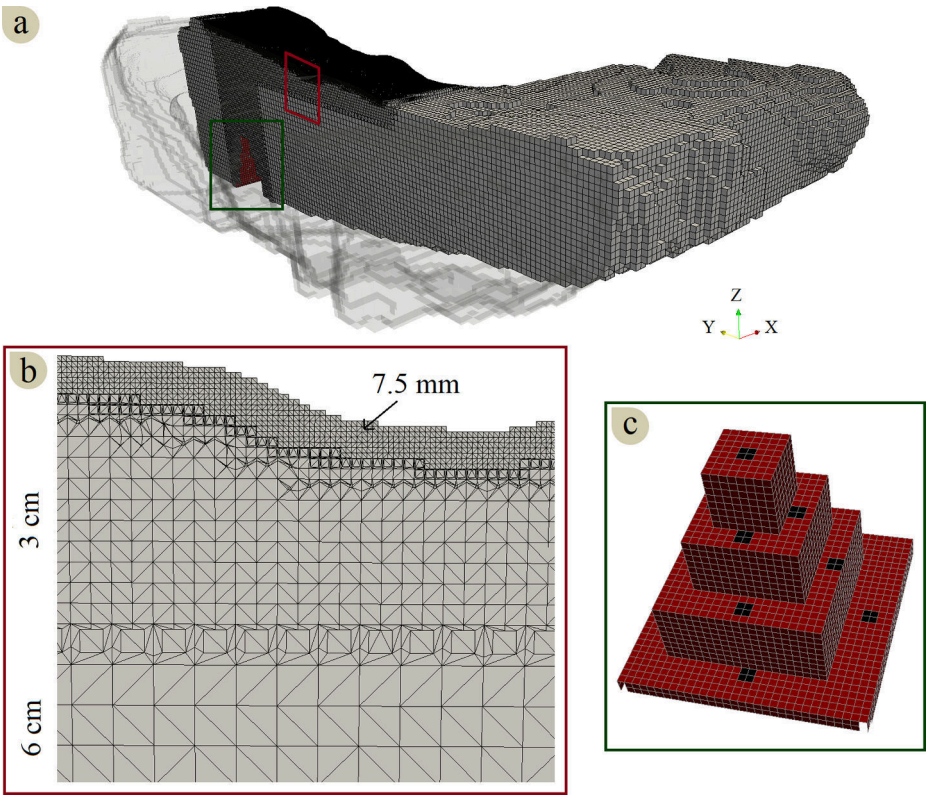

Fig. 6. a, Mesh of the quarry achieved with cfMesh (cfMesh, 2020). b, Zoom on the refinement associated with the ceiling jet flow. c, Pyramid-like numerical hearth. The HRR boundary condition is only applied on the black faces.

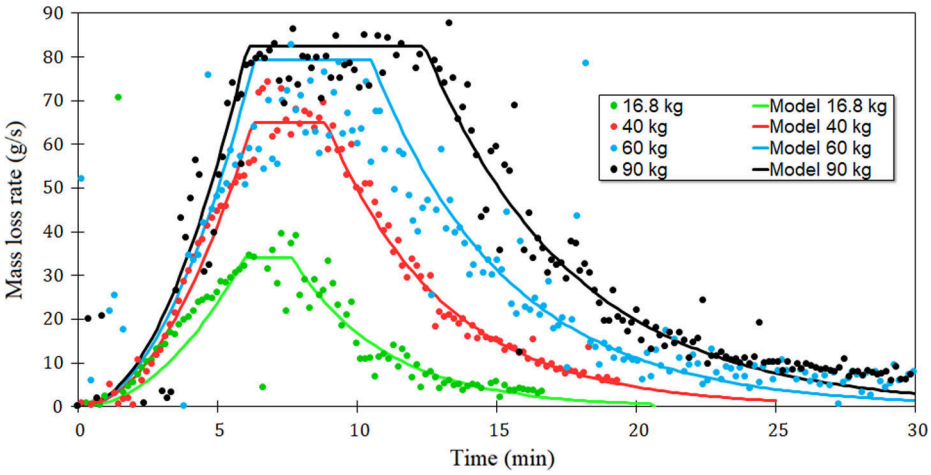

Fig. 7. Mass loss rates versus time for the four initial fuel masses. The model results (solid lines) are compared with the mass loss rate measurements (points).

applied to the burners (in black in Fig. 6c) for numerical reasons detailed in (Salmon et al., 2019a,b). In OpenFOAM, the HRR boundary condition is applied through the mass loss rate. Here, we imposed the mass loss rate calculated by our model which is based on the experiment (see Section 4.1)

Classical boundary conditions are applied to the quarry walls: zero Dirichlet boundary conditions for velocity and zero Neumann boundary conditions for mass fractions. The wall temperature is calculated from the following heat flux balance

$$q_r + h(T_g - T_w) = \lambda(T_w - T_x)/dx \tag{7}$$

where q_r is the radiative heat transfer at the wall, T_g is the gas temperature at the center of the boundary cell, T_w is the wall temperature, λ is the limestone thermal conductivity and T_x is the temperature within the wall, at the distance dx from the surface. The estimation of the convective heat transfer coefficient h depends on the configuration (Table 1). The wall temperature is calculated through the resolution of the 1D heat equation at each boundary face (Salmon, 2019). The rock mass contains water so the limestone properties must be modified accordingly. In particular, the vaporization of the water in rock is considered thanks to an increase of the specific heat at approximately 100 °C.

The initial temperature is 12 °C. This also corresponds to the temperature of the incoming air during all the simulation and the initial wall temperature. The humidity of air was also measured and imposed as 0.72% in the simulation.

FireFOAM is based on the finite volume method. The finite volume discrete ordinary method solves the radiative transfer equation over 32 solid angles. The resolution is achieved every ten flow iterations with a Courant number smaller than 0.8. A mesh decomposition over either 12 × 8 cores Intel Xeon E5-4640 2.4 GHz (case 1) or 20 × 24 cores Intel Haswell-EP Xeon 12-Cores E5-2690V3 2.6 GHz (case 2) is operated.

Table 1 summarizes the heat transfer modeling with numerical information for all the configurations.

Table 1
Heat transfer modeling (Section 3.3.2), number of cells and computational information for each studied configuration.

Configuration	Ceiling heat transfer	Walls heat transfer	Overall mesh size	Computer resources	Calculation time
1	(i)	(iii)	~1,540,000	Case 2	11 days
2	(ii)	(ii)	~340,000	Case 1	48 h
3	(iii)	(iii)	~340,000	Case 1	51 h

4. Results

4.1. Mass loss rate

This section handles the comparison between the mass loss rate measurements and the tailor-made model for tepee hearths (Section 3.1). Fig. 7 displays this comparison for the four fuel masses (16.8, 40, 60 and 90 kg). Each point corresponds to one measurement of mass loss rate, each color relates to one initial mass and the solid lines stand for the model results.

The construction of a model based on the conventional HRR curve is justified by the general trend of the mass loss rate. Indeed, this rate first nearly grows with the second power of time. Second, it reaches a limit depending on the initial mass. Finally, as expected, the decrease is not linear but this phase has been modified in the developed model.

The custom-made model provides very satisfactory mass loss rate thanks to the adjustment previously presented (Section 3.1). The exponential law enhances the description of the decreasing phase in comparison with the linear approximation of the conventional curve. Hence, there is an uncertainty of only 15% without considering the outliers (before 3 min 30) for the 90 kg hearth. In light of the complexity of wood combustion (Babrauskas, 2016), this gap is not significant and the simulation of this fire can rely on the model.

The black solid line (Fig. 8) is thus imposed as the boundary condition of the mass loss rate for the 90 kg hearth in the numerical simulation. We compare in Fig. 8 the experimental HRR under the hypothesis

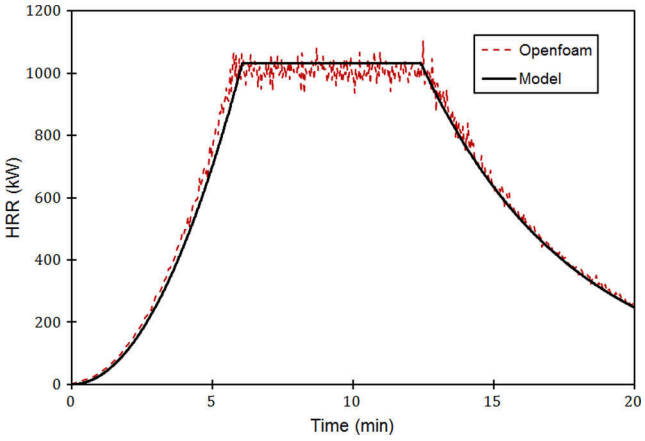

Fig. 8. Comparison between the modeled HRR prescribed as the boundary condition through the mass loss rate and the power released by the chemical reaction in the simulation.

that the heat of combustion remains constant ($HRR = \dot{m} \times \Delta H_c$ with ΔH_c the heat of combustion) with the numerical HRR (sum of the power released by the chemical reaction in each cell of the mesh).

The gap between the model and the numerical HRR is smaller than 5%. The input in the simulation corresponds therefore to the measurements with a good precision.

4.2. Ceiling jet

4.2.1. Experimental

The ceiling jet is defined as a shallow layer beneath the ceiling that only exists at the beginning of a fire while no stagnant hot layer exists (Alpert, 2016). However, Fig. 9 shows that such a layer has existed during the combustion of 90 kg of wood, especially close to the fire (T2).

As moving away from the hearth, this process lessens. For instance, the measurements at tree T4 only present a small temperature increase against the hot layer temperature. The thin hottest layer progressively merges with the so-called hot layer. Moreover, at the end of the fire, the energy release becomes insufficient to ensure the existence of the ceiling jet flow. This weakening is particularly observable on the measurements 15 min after the ignition.

The open geometry of the quarry seems to make the ceiling jet phenomenon possible because the hot gases are evacuated and cold air can supply the fire. Therefore, the gases are moving and no quiescent hot layer takes place. The latter then cannot fully prevent the ceiling jet flow. Note that the confinement, which is significant (Fig. 1), does not avoid this process either.

Regarding the comparison with the empirical correlations, tree T4 is not in the same gallery as the fire and tree T2 is too close to the hearth ($Y < 1.6$ m) to be in the validity range of Delichatsios' correlation. Therefore, only the measurements of tree T3 can be discussed. Table 2 compares the maximum measured temperature in the ceiling jet flow at tree T3 with the temperature calculated from Delichatsios' correlation associated with the corrections introduced by Cooper and Evans (Section 3.2). Three times are considered: 5, 10 and 15 min after ignition.

Table 2
Maximum ceiling jet temperatures according to the measurements and Delichatsios' correlation associated with the Evans and Cooper corrections. The gaps between measurements and calculations are given next to the temperatures. The comparison is made for tree T3 (Fig. 9).

Time after ignition	Measurement	Delichatsios - Evans | Gap with measurements	Delichatsios – Cooper | Gap with measurements
5 min	457 °C	461 °C | 1%	450 °C | 2%
10 min	526 °C	543 °C | 3%	529 °C | 1%
15 min	425 °C	448 °C | 5%	438 °C | 3%

The maximum temperatures given by the correlation agree with the measurements. The gap remains smaller than 5% for both corrections. The good agreement shows that the correlation and the corrections are suitable for this configuration. Therefore, the small slope of the quarry ceiling negligibly impacts the temperature of the ceiling jet since it matches with the prediction for plate ceilings.

4.2.2. Simulation

The only configuration where the ceiling jet flow is simulated corresponds to the first one (Table 1). Since tree T4 is not associated with any refinement in the simulation (Section 3.3.3), only the comparison for trees T2 (Fig. 10) and T3 (Fig. 11) is considered in this section. In these figures, the solid lines stand for the calculated temperatures, the dashed lines represent the measurements and the points correspond to the vertical locations of the thermocouples.

There is a good agreement between simulation and experiment 15 min after ignition. The numerical profile looks very similar to the measurements with consistent temperatures. The gap between the

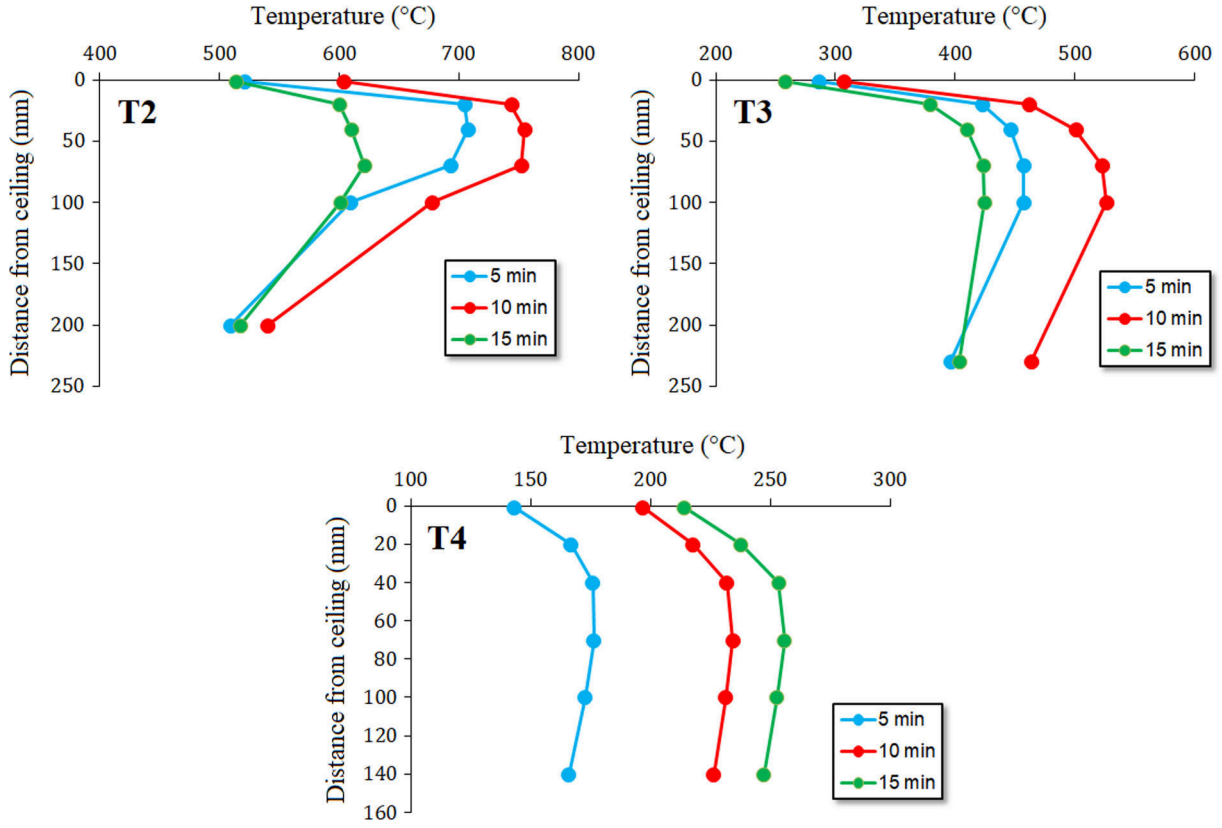

Fig. 9. Measured temperatures in the ceiling jet flow at trees T2, T3 and T4 five, ten and fifteen minutes after the ignition of the 90 kg hearth. The points stand for the locations of the sensors, which are also indicated in Fig. 4.

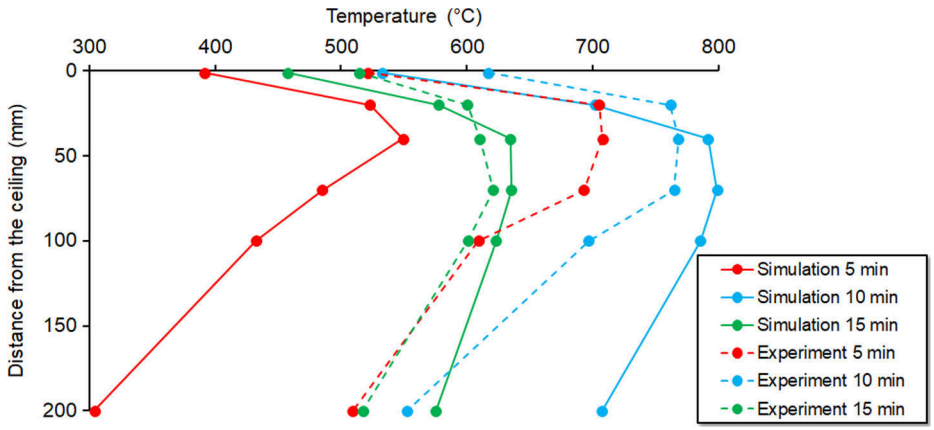

Fig. 10. Numerical and experimental temperature profiles near the ceiling at tree T2.

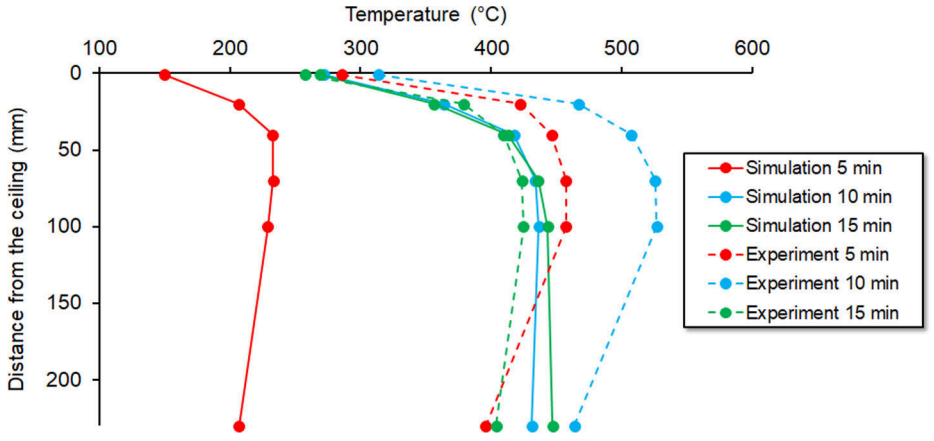

Fig. 11. Numerical and experimental temperature profiles near the ceiling at tree T3.

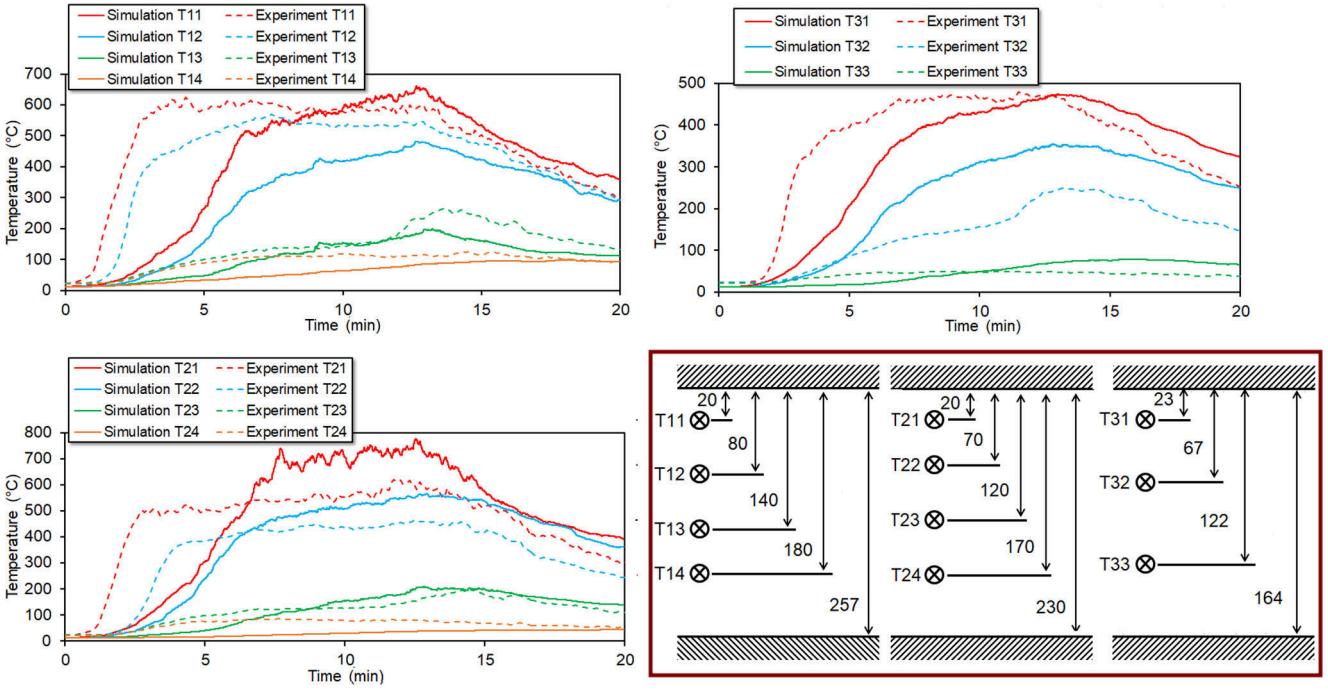

Fig. 12. Numerical and experimental temperatures for configuration 1. The distances are given in cm.

calculation and data is equal to 6% at tree T2 and smaller than 5% at tree T3. 10 min after ignition, the simulation also provides satisfactory results, especially at tree T2. The temperature profile is close to the data since the gap is smaller than 12% while the difference is approximately 16% at tree T3. Note that such deviations are reasonable for this kind of phenomena which are known to be difficult to simulate (Chatterjee et al., 2017).

At both locations, 5 min after ignition, the simulation widely underestimates temperature. As we will see in Section 4.3.1, this observation is not specific to the ceiling jet but corresponds to a global discrepancy. The miscalculation of the HRR could be at the root of this problem. Indeed, the HRR is computed from the mass loss rate and the heat of combustion. The latter is supposed to remain constant during the combustion process. The experimental data seem to show that this simplifying assumption is wrong. According to Fig. 7, the maximum mass loss rate is reached after 6 min. However, the thermocouples began to measure the maximum level of temperature just 3 min after ignition (Fig. 12). This suggests that the power released by the fire was maximum 3 min after ignition contrary to the numerical input. The large deviation could thus simply stem from the assumption regarding the heat of combustion.

The deviation from the experimental data is therefore smaller than 20% and rather close to 10%. Considering the complexity of the problem (relatively large 3D irregular geometry and powerful fire) and the refinement which is not particularly significant, this error appears low. Besides, we can expect results closer to experimental data with a more refined mesh. However, if one is only concerned by ceiling jet, the Delichatsios correlation should be preferred.

4.3. Global temperatures

This section addresses the comparison between the measurements and the numerical temperatures calculated in the three configurations detailed in Table 1. Only the temperatures outside the ceiling jet area are considered and the discussion focuses on trees T1, T2 and T3 (Fig. 3). Fig. 4 displays the vertical locations of the thermocouples for each tree.

4.3.1. Configuration 1

This configuration corresponds to the most refined one and is not concerned by any hypothesis contrary to configuration 3 (Table 1). Fig. 12 displays both the numerical and experimental temperatures at the measurement points. Each graph relates to one tree of thermocouples and their locations are given in the bottom right picture.

The experimental temperatures near the ceiling (T11, T21 and T31) sharply increase between two and three minutes after ignition. As previously mentioned (Section 4.2.2), the mass loss rate measurements present a less acute slope over the first 6 min. Therefore, the energy released by the fire is not exactly proportional to the mass loss rate because the heat of combustion should have varied with time. Such a variation has already been measured by other scientists. In Browne and Brenden (1964), the authors measured the heat of combustion of the volatile pyrolysis products of ponderosa pine. After 10% weight loss, the heat of combustion is equal to 11 kJ/kg, whereas after 60% weight loss, it is equal to 14.2 kJ/g. Babrauskas (2008) also observed variations in the composition of the volatile products during the combustion of western red cedar. There was a peak (17 kJ/g) at the beginning before reaching a value that remained constant until the end (without considering char combustion). He therefore measured a decrease contrary to Browne and Brenden. Here we did not measure the heat of combustion of the volatile pyrolysis products of scots pine.

Its variation is out of the purpose of the paper so the heat of combustion has been considered as a constant in the simulation. The underestimation of the energy released by the fire is approximately 10%. With the goal of applying our model to the Chauvet-Pont d'Arc Cave, this error is not prohibitive for assessing the order of magnitude of the wood masses.

This means that the first 6 min of the numerical results are not reliable. However, the experimental trend after this first part is the same as the simulated one (Fig. 12). Therefore, the assumption on the heat of combustion seems to be consistent after the beginning.

In the second phase of the fire, which corresponds to the constant release of energy, the simulated temperatures are close to the measurements, especially in the hot layer. Only T21 presents a non-negligible deviation of 25%. The thermocouples associated with the blue curves were located in a high temperature gradient area. A difference of a few centimeters on the believed position of the thermocouples could explain the gap between experimentation and simulation. The physical location of the thermocouples in the quarry is subject to uncertainties but they cannot exceed one centimeter in height. However, considering the inaccuracies involved by the meshing process and the size of the cells, it is not possible to guarantee that the location of the thermocouples is exactly the same as in the simulation. Indeed, the inaccuracy on the ceiling height is directly linked to the size of the cells at the ceiling and on the ground. The position of the thermocouples could thus suffer from an uncertainty of a few centimeters in the simulation. Thus, any conclusion about the thermocouples in such zones is unreliable. We highlight that the main inaccuracy is the match of the thermocouple locations in the experiment and the simulation. The measurement uncertainty inherent in the thermocouples is smaller than 5 °C. The lowest thermocouples remained at rather weak temperatures in both the simulation and the experiment. The simulation is therefore of a satisfactory level in the cold layer.

The decreasing phase displays a good agreement between the measured and calculated trends. Indeed, the gaps observed during the second phase of the fire remain the same in the last phase. The end of the fire is thus rather accurately simulated, partly thanks to the exponential law describing the mass loss rate (Section 3.1).

The results given in Fig. 12 show that FireFOAM can manage very complex fires in irregular geometries, provided that the mesh is fine enough. In the next section, we show that a very refined mesh is a necessary condition to get consistent results.

4.3.2. Configuration 2

This configuration (Table 1) is very usual in the papers dealing with compartment fires (particularly with FDS). The mesh is quite fine with 3 cm and 6 cm cubic cells (Section 3.3.3), but the ceiling jet area is not refined because it is not necessarily of interest in these studies. With the same graphic convention, Fig. 13 presents the results for the three trees in configuration 2.

This configuration fails to give consistent temperatures. The detailed comparison for each thermocouple is not proposed here since the quality of all the numerical results is poor. Overall, the temperature is significantly underestimated by the simulation. The reasons of this failure were provided in (Salmon et al., 2019a,b) without demonstrating them on a test case. The main issue in this kind of simulation is the non-refinement of the ceiling jet area. This zone concentrates a great part of the energy released by the fire. With 3 cm cubic cells, the calculated temperature is averaged on 3 cm. However, high temperature gradients take place in this area so assuming that the temperature remains constant over 3 cm is not appropriate. Such a mesh thus induces a numerical diffusion of energy and then an underestimation of the temperature. Since there is a great amount of energy in the ceiling jet zone, the loss is meaningful. In addition, the low temperature of the gases entails an underestimation of the wall temperature. Then, the radiation of the walls is weaker than expected. Finally, Newton's law of cooling also leads to incorrect heat transfers. Being based on the gas temperature, this law cannot properly assess the convective heat transfer.

Even if the study is not concerned by ceiling jet, a fire occurring in an open compartment such as the quarry (Fig. 1), requires the ceiling jet area to be refined in a classical simulation with FireFOAM. FDS seems to avoid this problem since it reaches consistent temperatures without refinement. The adjustment of coefficients on many experiments could

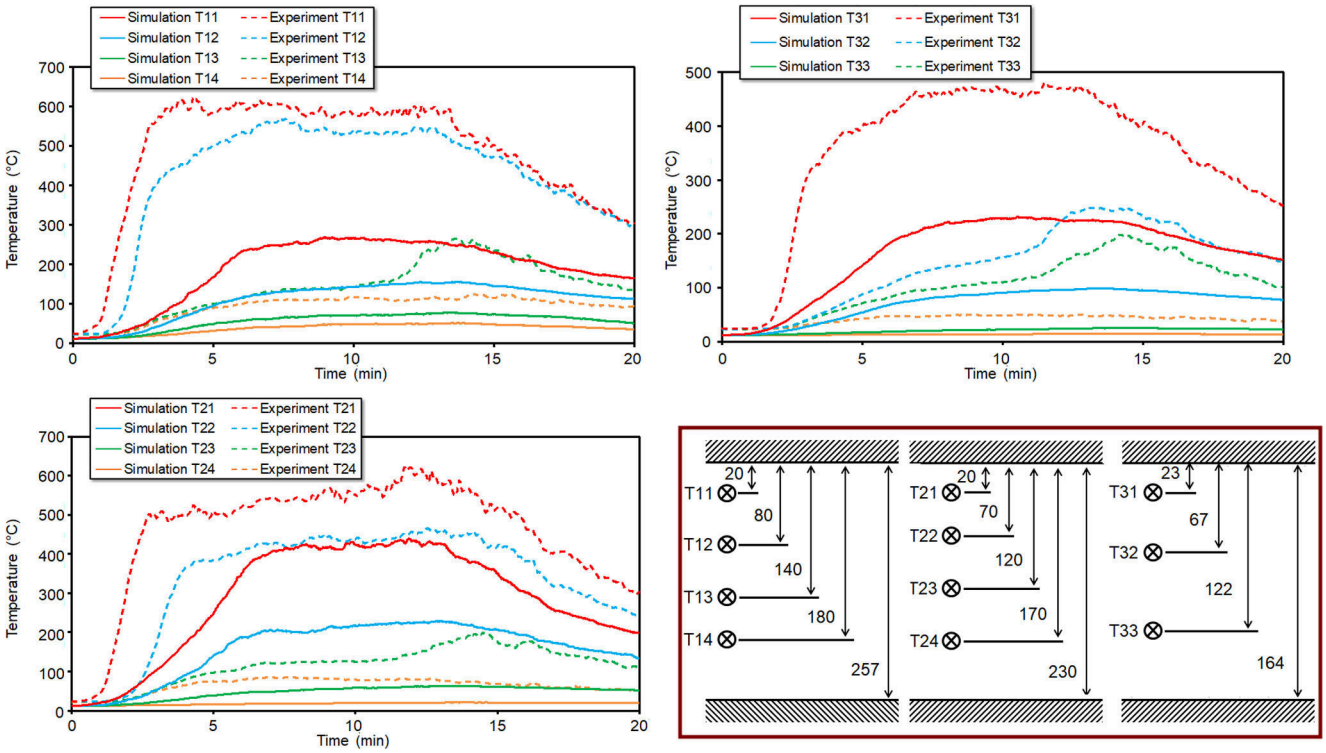

Fig. 13. Numerical and experimental temperatures for configuration 2. The distances are given in cm.

be at the source of this behavior.

In the next section, another approach with FireFOAM, based on simplifying assumptions, leads to quite accurate results without such a refinement in the ceiling jet zone.

4.3.3. *Configuration 3*

The same mesh as that of configuration 2 is used (Table 1). This mesh was selected based on a grid convergence study presented in (Salmon, 2019). To circumvent the problem of configuration 2, we enforce the vertical gas velocity to be equal to zero outside the turning region (see

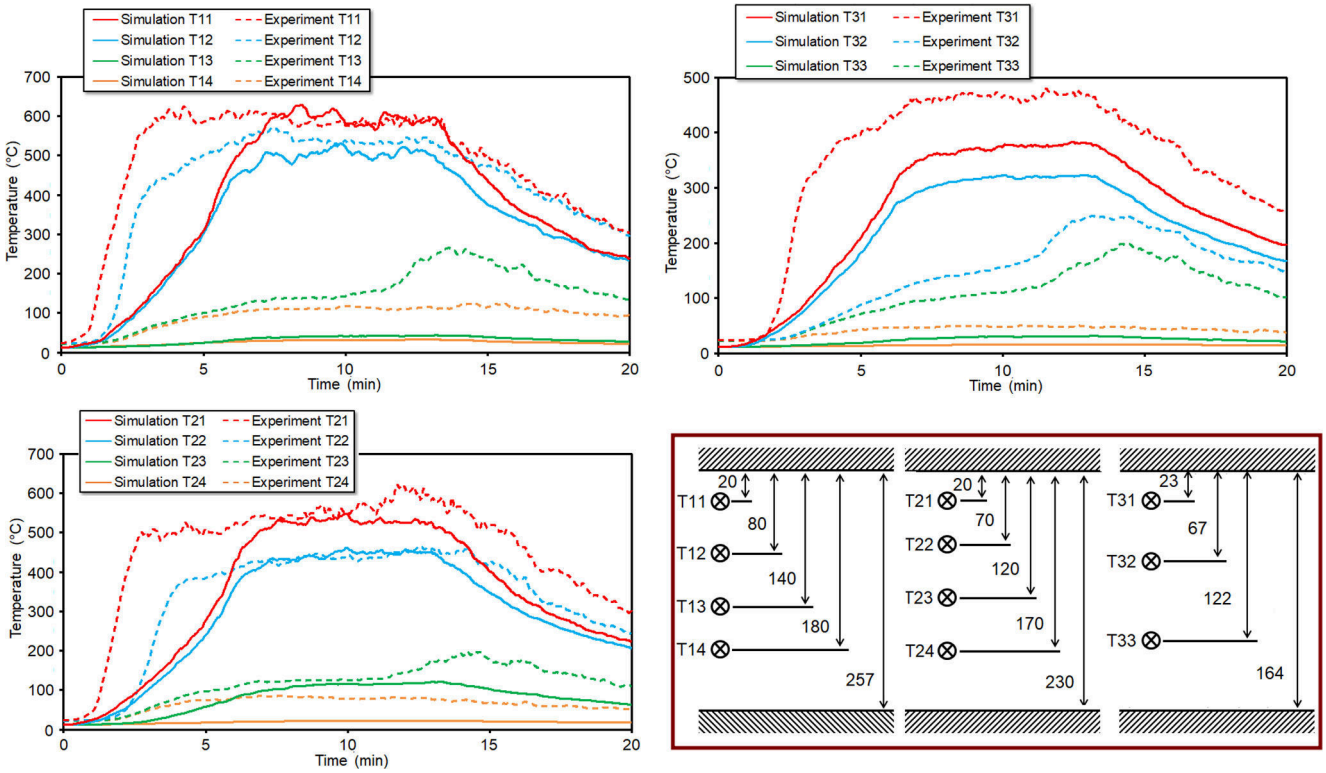

Fig. 14. Numerical and experimental temperatures for configuration 3. The distances are given in cm.

(Salmon et al., 2019a,b) for details). This approach limits the vertical spreading of energy. Then, the temperature of the hot layer is greater. However, the coarse mesh near the walls, where very high temperature gradients take place due to boundary layers and the ceiling jet phenomenon, does not yield precise heat transfer calculations. Therefore, this configuration requires a tailor-made heat transfer modeling. Here, we use model (iii) (Section 3.3.2), which is thoroughly described in (Salmon et al., 2019a,b). Fig. 14 compares the simulation with the measurements.

As expected, one can notice that the hot layer is warmer in this simulation than in configuration 2. Trees T1 and T2 present a very good agreement between simulation and experimentation in the hot layer. There is a little deviation at tree T3 but while the highest thermocouple (red curve) measured warmer temperatures than in the simulation (20%), the next one (blue curve) was colder than the calculated temperature. As mentioned for configuration 1, there are high temperature gradients and only a gap of a few centimeters could modify a lot the measured temperatures.

The weakness of the simplifying assumptions is the underestimation of the temperature of the cold layer. Due to the hypothesis about the vertical velocity, the heat transfer from the hot layer to the cold one is smaller in the simulation. For the three trees, the temperature of the colder thermocouples computed from the simulation remains almost equal to the ambient temperature. This deviation could depend on the intensity of the fire. Here, the maximum HRR, which is approximately 1 MW, is most of the time higher than in a prior paper where the assumptions were also applied (Salmon et al., 2019a,b). In this previous paper, the inaccuracy of the simulation in the cold layer is less obvious. Therefore, the assumption on the vertical velocity seems to work better with low energy releases, when there is a clear distinction between the hot and cold layers. In that respect, it seems that this hypothesis requires a thermal stratification to be applicable. When the gas distribution does not meet this behavior, a simulation such as that of configuration 1 should be preferred.

5. Conclusion

In order to give clues on the fires conducted in the Chauvet-Pont d'Arc Cave, we have developed a modeling strategy of wood fires in confined geometries. For this purpose, we successively carried out four experimental fires in a former limestone quarry. 27 thermocouples were set up in the quarry (mostly close to the fires and in the ceiling jet area) and a weighing scale was placed under the burning hearths.

A modeling of the mass loss rate of tepee-like hearths has been constructed. The parameters of the model have been built as a function of the initial mass of the hearth. The comparison between this approach and the mass loss rate measurements demonstrates the suitability of our adjusted model.

We have also compared different kinds of simulation with measurements. Even if the choice of the modeling depends on the aim of the study, configuration 2 (intermediate refinement) is not a viable solution for confined and ventilated fires. The existence of a ceiling jet necessarily requires a great refinement, even to compute the temperature outside this area. Configuration 1 (high refined) gives satisfactory results considering the complexity of such a study. However, the calculations associated with refined meshes demand high-performance computing facilities and time (11 days for simulation 1). This prohibits the widespread use of this approach. The development of simplifying assumptions makes possible the simulation of this kind of fires with manageable mesh sizes (configuration 3). They allow us to reach, in two days and five times less processors than in configuration 1, temperatures about as precise as with high refinement.

In the ceiling jet area, the measured temperatures have been confronted with the corrected Delichatsios correlations and the simulation. The Cooper and Evans corrections of the Delichatsios correlation yield suitable maximum temperatures in agreement with the experiment. The FireFOAM simulation, based on a mesh refined in the ceiling jet area, also provides consistent order of magnitudes. It is worth noting that the empirical correlations give more accurate temperatures than the simulation.

Our investigation being focused on the Chauvet-Pont d'Arc Cave, many fire scenarios must be run to understand which fires occurred at the thermo-altered areas. Therefore, configuration 3 seems to be the best choice to perform these simulations while configuration 1 would be rather dedicated to studies with single simulations. The mass loss rate model and the prior investigations (Salmon et al., 2019a,b) will make possible the determination of the mass of wood burnt in the Chauvet-Pont d'Arc Cave. Beyond this archaeological purpose, this study could help for numerical engineers and researchers in the simulation of complex compartment fires. In that regard, the methodology can also be applied to fires in tunnels, underground mining galleries, car parks or confined rooms such as in buildings for instance. In such studies, configuration 1 is the safest approach but also the most time-consuming. As regards configuration 3, one should ensure that there is a thermal stratification for the velocity hypothesis to be reliable.

CRediT authorship contribution statement

F. Salmon: Writing - original draft. **J.-C. Mindeguia:** Writing - review & editing. **D. Lacanette:** Writing - review & editing. **C. Sirieix:** Writing - review & editing. **J.-C. Leblanc:** Writing - review & editing. **C. Ferrier:** Writing - review & editing.

Declaration of Competing Interest

The authors declare that they have no known competing financial interests or personal relationships that could have appeared to influence the work reported in this paper.

Acknowledgement

We thank the Regional Council of Aquitaine and Nouvelle-Aquitaine for providing funding for the CarMoThap project and for their investment in a 432-processor cluster located in the I2M laboratory. The researches on the Chauvet-Pont d'Arc Cave have received specific financial help from the French Ministry of Culture and Communication. We thank the LCPP staff (Laboratoire Central de la Préfecture de Police) for their help in providing the experimental instrumentation (velocity sensors, thermocouples, gas and particle concentration sensors). Furthermore, the following institutions have given support: CNRS, Bordeaux University, Bordeaux-INP and Bordeaux-Montaigne University. We thank C. Bouchet, the owner of the quarry in Fauroux (Lugasson) and M. Vidal for having made available scots pine, as well as the SDIS 33 staff for participation in the experiments of the CarMoThaP program. This work was also performed using HPC resources from GENCI-CINES (Grant 2017- A0032B10268).

References

Alpert, R., 1975. Turbulent ceiling-jet induced by large-scale fires. Combust. Sci. Technol. 11 (5–6), 197–213.
Alpert, R., 2016. SFPE Handbook of Fire Protection Engineering, chapter Ceiling Jet Flows. Springer, s.l.
Babrauskas, V., 2008. The cone calorimeter. SFPE Handbook of Fire Protection Engineering. Springer, s.l.
Babrauskas, V., 2016. SFPE Handbook of Fire Protection Engineering, chapter Heat Release Rates. Springer, s.l.
Betting, B., et al., 2018. Experimental and Numerical investigations of the flow characteristics in confined fires. J. Phys. Conf. Ser. 1107 (4), 042015.
Beyler, C., 1986. Fire plumes and ceiling jets. Fire Saf. J. 11 (1–2), 53–75.
Brodard, A. et al., 2014. Les rubéfactions des parois de la grotte Chauvet : une histoire de chauffe ?. chez Les arts de la Préhistoire : micro- analyses, mises en contextes et conservation, Paillet P. (dir), 2014.
Browne, F., Brenden, J., 1964. Heats of combustion of the volatile pyrolysis products of ponderosa pine. US Forest Service Research Paper FPL 19, Volume US Department of Agriculture.

Caliendo, C., et al., 2013. Simulation of fire scenarios due to different vehicle types with and without traffic in a bi-directional road tunnel. Tunn. Undergr. Space Technol. 37 (1), 22–36.
cfMesh, 2020. cfMesh. http://cfmesh.com.
Chatterjee, P., Meredith, K., Wang, Y., 2017. Temperature and velocity distributions from numerical simulations of ceiling jets under unconfined, inclined ceilings. Fire Saf. J. 91, 461–470.
Chen, C., Zhang, Y., Lei, P., Jiao, W., 2020. A study for predicting the maximum gas temperature beneath ceiling in sealing tactics against tunnel fire. Tunn. Undergr. Space Technol. 98 (103275).
Cooper, L., 1984. A Buoyant Source in the Lower of Two Homogeneous, Stably Stratified Layers. Combustion Institute, Pittsburgh.
Debard, E., Ferrier, C., Kervazo, B., 2012. Etude géologique de la grotte Chauvet-Pont d'Arc. Bilan des travaux de la triennale 2010-2012. Etudes pluridisciplinaires à la grotte Chauvet-Pont d'Arc (Ardèche). Rapport d'activité 2010-2012, vol. 1, pp. 59–98.
Delichatsios, M., 1981. The flow of fire gases under a beamed ceiling. Combust. Flame 43, 1–10.
Evans, D., 1985. Calculating sprinkler actuation time in compartments. Fire Saf. J. 9 (147).
Ferrier, C., et al., 2014. Les parois chauffées de la grotte Chauvet-Pont d'Arc (Ardèche): caractérisation et chronologie. Paléo 25, 59–78.
FireFOAM, 2020. FireFOAM. http://www.fmglobal.com/modeling.
Guibert, P., et al., 2015. When were the walls of the Chauvet Pont-d'Arc Cave heated ? A chronological approach by thermoluminescence. Quat. Geochronol. 29, 36–47.
Hara, T., Kato, S., 2006. Numerical simulation of fire plumes-induced ceiling jets using the standard kε model. Fire Technol. 42 (2), 131–160.
He, Q., Yang, J., Zhang, Y., 2018. Numerical simulation of fire induced gas flow in a narrow ceiling vented compartment. Procedia Eng. 211, 226–234.
Holman, J., 2010. Heat Transfer (Tenth edition). McGraw-Hill Series in Mechanical Engineering.
Hsu, W., et al., 2017. Analysis of the Hsuehshan Tunnel Fire in Taiwan. Tunn. Undergr. Space Technol. 69, 108–115.
Huo, Y., Gao, Y., Chow, W., 2015. A study on ceiling jet characteristics in an inclined tunnel. Tunn. Undergr. Space Technol. 50, 32–46.
Ingason, H., 2009. Design fire curves for tunnels. Fire Saf. J. 44 (2), 259–265.
Ingason, H., Li, Y., Lönnermark, A., 2015. Tunnel Fire Dynamics. Springer.
Jayatilleke, C., 1969. The influence of Prandtl number and surface roughness on the resistance of the laminar sub-layer to momentum and heat transfer. Progress Heat Mass Transfer 1, 193–329.
Johansson, N., Wahlqvist, J., Hees, P.V., 2015. Numerical experiments in fire science: a study of ceiling jets. Fire Mater. 39, 533–544.
Lacanette, D., et al., 2017. Simulation of an experimental fire in an underground limestone quarry for the study of Paleolithic fires. Int. J. Therm. Sci. 120, 1–18.
Le, D., et al., 2018. Assessment of the capabilities of FireFOAM to model large-scale fires in a well-confined and mechanically ventilated multi-compartment structure. J. Fire Sci. 36 (1), 3–29.
Liu, F., Yu, L., Weng, M., Lu, X., 2016. Study on longitudinal temperature distribution of fire-induced ceiling flow in tunnels with different sectional coefficients. Tunn. Undergr. Space Technol. 54, 49–60.
Magnussen, B., Hjertager, B., 1977. On mathematical modeling of turbulent combustion with special emphasis on soot formation and combustion. Proc. Combust. Int 719–729.
McGrattan, K. et al., 2013. Fire Dynamics Simulator User's Guide, Sixth edition 1019. [Online] Available at: https://pages.nist.gov/fds-smv/manuals.html.
Meng, N., et al., 2014. Numerical study on the optimization of smoke ventilation mode at the conjunction area between tunnel track and platform in emergency of a train fire at subway station. Tunn. Undergr. Space Technol. 40, 151–159.
Mindeguia, J., Carré, H., Pimienta, P., Borderie, C.L., 2015. Experimental discussion on the mechanisms behind the fire spalling of concrete. Fire And Materials 39, 619–635.
Oka, Y., Ando, M., 2013. Temperature and velocity properties of a ceiling jet impinging on an unconfined inclined ceiling. Fire Saf. J. 55, 97–105.
Quiles, A., et al., 2016. A high-precision chronological model for the decorate Upper Paleolithic cave of Chauvet-Pont d'Arc, Ardèche, France. Proc. Natl. Acad. Sci. 113 (17), 4670–4675.
Salmon, F., 2019. Aero-thermo-mechanical simulation of fire effects on the walls of a confined space : application to the thermo-alterations of the Chauvet-Pont d'Arc Cave, PhD Thesis, Université de Bordeaux.
Salmon, F., et al., 2018. FireFOAM simulation of a localised fire in a gallery. J. Phys. Conf. Ser. 1107 (042017).
Salmon, F., et al., 2019a. Development of a fluid-structure coupling validated with a confined fire: application to painted caves. Fire Technol. 56 (3), 1197–1227.
Salmon, F., et al., 2019b. Localized fire in a gallery: model development and validation. Int. J. Therm. Sci. 139, 144–159.
Spalding, D., 1961. A Single Formula for the "Law of the Wall". J. Appl. Mech. 28, 455–458.
Tang, F., Chen, L., Chen, Y., Pang, H., 2020. Experimental study on the effect of ceiling mechanical smoke extraction system on transverse temperature decay induced by ceiling jet in the tunnel. Int. J. Therm. Sci. 152 (106294).
Théry-Parisot, I., et al., 2018. Illuminating the cave, drawing in black: wood charcoal analysis at Chauvet-Pont d'Arc. Antiquity 92 (1362), 320–333.
Walter, D., Buxbaum, G., Laqua, W., 2001. The mechanism of the thermal transformation from goethite to hematite. J. Therm. Anal. Calorim. 63, 733–748.
Yao, Y., et al., 2018. Maximum gas temperature rise beneath the ceiling in a portals-sealed tunnel fire. Tunn. Undergr. Space Technol. 80, 10–15.
Yao, Y., et al., 2019. Study of tunnel fires during construction using a model scale tunnel. Tunn. Undergr. Space Technol. 89, 50–67.
Ye, K., et al., 2019. Estimating the longitudinal maximum gas temperature attenuation of ceiling jet flows generated by strong fire plumes in an urban utility tunnel. Int. J. Therm. Sci. 142, 434–448.
Yoshizawa, A., 1986. Statistical theory for compressible turbulent shear flows, with the application to subgrid modeling. Phys. Fluids 29 (7), 2152–2164.
Zadeh, S., Maragkos, G., Beji, T., Merci, B., 2016. Large eddy simulations of the ceiling jet induced by the impingement of a turbulent air plume. Fire Technol. 52 (6), 2093–2115.
Zhao, S., et al., 2018. A numerical study on smoke movement in a metro tunnel with a non-axisymmetric cross-section. Tunn. Undergr. Space Technol. 73, 187–202.